Chemical Science

ROYAL SOCIETY OF CHEMISTRY

EDGE ARTICLE

View Article Online
View Journal | View Issue

Cite this: *Chem. Sci.*, 2025, **16**, 11858

All publication charges for this article have been paid for by the Royal Society of Chemistry

Flexible phosphonium and sulfonate pair-to-pair self-assembled ionic organic single crystals for iodine capture†

Mingxia Sun,[ab] Jia Chen,[*ab] Ting Zhang,[a] Wei Xu,[ab] Jing He,[ab] Yunyun Zhang,[ab] Huifeng Liu,[a] Shuang Zhang,[a] Juanjuan Wang,[a] Xin Li,[a] Yali Yang[a] and Hongdeng Qiu[*abc]

Received 15th March 2025
Accepted 21st May 2025

DOI: 10.1039/d5sc02039e

rsc.li/chemical-science

In this work, four flexible chain phosphonium-based ionic organic single crystals (IOCs) are first facilely prepared by pair-to-pair ionic self-assembly of phosphonium salts and sulfonic acids (salts) under mild conditions. Their structures, morphology, stability, and surface areas are characterized in detail. Featuring a wealth of sulfonate and phenyl groups as powerful active sites for iodine adsorption, these materials exhibit considerable capture capacities. An in-depth investigation of the adsorption mechanism reveals that iodine adsorption on these materials occurs in three distinct states (I_2, I_3^-, and I_5^-) and follows a mixed-mode adsorption process, involving both physical and chemical interactions. Consequently, this study not only presents a new kind of single crystalline material based on flexible phosphonium and sulfonic anionic pairs, but also significantly hints at the application possibility of this kind of IOC in some other fields.

Introduction

Nuclear energy is increasingly recognized as a sustainable and non-greenhouse gas-emitting energy source.[1–4] However, the environmental and biological risks posed by radioactive elements within nuclear waste present considerable challenges in its management.[5–7] Among nuclides, ^{129}I has garnered significant attention due to its toxicity, an extended half-life of approximately 1.6×10^7 years, and its high mobility across various geological settings.[8] Additionally, another isotope of iodine, ^{131}I, although characterized by a relatively short half-life of 8.02 days, emits intense radiation and has the potential to readily contaminate the environment. Such contamination can lead to detrimental effects on human metabolic processes.[9] Consequently, the development of adsorbents capable of efficiently sequestering iodine and facilitating its long-term storage is crucial for mitigating the risks associated with radioactive iodine contamination.[10]

Currently, a diverse array of adsorbent materials is employed for the capture of iodine, encompassing conventional adsorbents such as activated carbon,[11–13] graphene,[14,15] and a range of innovative organic supramolecular materials, including metal–organic frameworks (MOFs),[16–19] covalent organic frameworks (COFs),[20–24] hydrogen-bonded organic frameworks (HOFs),[25–27] porous organic polymers (POPs),[28–32] and porous organic cages (POCs).[10,33–35] Despite their utility, these materials confront challenges related to selective molecular capture and the long-term stability of the adsorbent due to their inherent fixed porosity and the relatively weak van der Waals interactions between the guest molecules and the porous frameworks. Furthermore, the solubility of these materials is compromised by their rigid, cross-linked macromolecular structures, which impedes their processability in solution.

In 2008, Wathier *et al.*[36] introduced the concept of a "supramolecular ionic network," which is a new kind of novel material, through the self-assembly of multivalent cationic and anionic molecular pairs. Unlike coordination bonds and covalent bonds with fixed directions, the flexibility of electrostatic force can provide multiple structural possibilities to the system.[37] Based on the charge characteristics of ionic bonds in monomers and the designability of organic groups, functional groups, active adsorption sites, and physical and chemical properties of the materials can be adjusted according to the needs. This enables the design and preparation of ionic supramolecular network materials with rich structure and properties. Recent advances in this field have seen the creation of ionic supramolecular networks using imidazolium[38] and

[a]*CAS Key Laboratory of Chemistry of Northwestern Plant Resources and Key Laboratory for Natural Medicine of Gansu Province, Lanzhou Institute of Chemical Physics, Chinese Academy of Sciences, Lanzhou, 730000, China. E-mail: jiachen@licp.cas.cn; hdqiu@licp.cas.cn*

[b]*University of Chinese Academy of Sciences, Beijing, 100049, China*

[c]*Key Laboratory of Rare Earths, Ganjiang Innovation Academy, Chinese Academy of Sciences, Ganzhou, 341000, China*

† Electronic supplementary information (ESI) available. CCDC 2415289–2415292. For ESI and crystallographic data in CIF or other electronic format see DOI: https://doi.org/10.1039/d5sc02039e

pyridium[39–41] as ionic bonding sites, demonstrating the potential of this approach. However, the synthesis of ionic organic single crystals (IOCs) using phosphonium salts has not yet been reported, which suggests an area for future research and development. The use of sulfonic acid is particularly intriguing, as it is a strong acid that readily ionizes in polar solvents, thus providing a source of charged monomers that can readily combine with cationic monomers to form IOCs. Heteroatoms present in sulfonic acid can also interact with a wide array of target analytes,[42–44] which enhances the versatility and applicability of these materials for adsorption purposes.

In this work, four flexible phosphonium-based ionic crystals were synthesized using two bisphosphonium salts with different alkyl chain lengths and three sulfonate compounds at room temperature for 12 h for the first time. This synthetic approach diverges from conventional single crystal preparation techniques, such as volatilization, liquid diffusion, and gas diffusion, by facilitating the direct pair-to-pair assembly of the two monomeric constituents in solution. The crystallographic data of the four materials were characterized by single crystal diffraction, the apparent morphology, crystal shape, and thermal stability of the materials were tested by using optical microscopy, X-ray diffraction (XRD), thermogravimetric analysis (TGA), and an automatic surface and porosity analyzer and specific surface area was calculated with the Brunauer, Emmett, and Teller (BET) equation. To investigate the influence of distinct crystal structures on iodine adsorption efficiency, the adsorption properties of these four materials were systematically evaluated under uniform conditions. To elucidate the mechanisms governing iodine adsorption onto the synthesized phosphonium-based ionic crystals, an array of advanced characterization methods was utilized. These included TGA, X-ray photoelectron spectroscopy (XPS), Fourier transform infrared spectroscopy (FT-IR), Raman spectroscopy, and energy dispersive X-ray spectroscopy (EDS), applied sequentially before and after the iodine adsorption process. Furthermore, density functional theory (DFT) calculations have substantiated the significant contributions of the sulfonic acid group and the benzene ring in facilitating the iodine adsorption mechanism. This ensemble of data provided insights into the adsorption behavior at the material's and the physical and chemical interactions occurring during the adsorption process.

Results and discussion

Synthesis of four IOCs

Two flexible commercially available phosphonium salts including phosphonium, 1,1′-(1,2-ethanediyl)bis[1,1,1-triphenyl-, bromide] (PEBT) and phosphonium, 1,1′-(1,4-butanediyl)bis[1,1,1-triphenyl-bromide (PBBT) were used, while three different sulfonic acids including 1,5-naphthalenedisulfonic acid (NDS), 1,3,6,8-pyrenetetrasulfonicacid, sodium salt (PTS), and 4,4′-biphenyldisulfonic acid (BDS) were used as anionic pairs.

The phosphonium salts and sulfonic acids were each dissolved in their respective solvents. Following this, the two solutions were combined and allowed to stand at room temperature for a duration of 12 h during which the IOCs formed. Notably, during the anion/cation pairing that leads to the formation of single crystals, four different flexible-phosphonium IOCs including PEBT-NDS, PEBT-PTS, PBBT-PTS and PBBT-BDS were obtained. The detailed preparation parameters and synthesis process for these materials are depicted in Scheme 1 and Table S1.†

Crystal structures

Fig. 1 and Table S2† provide detailed schematic representations of the structure and cell parameters of the four IOCs. PEBT-NDS (CCDC No. 2415289) is classified within the triclinic crystal system, $\bar{1}$ point group, and $P\bar{1}$ space group. The illustration in

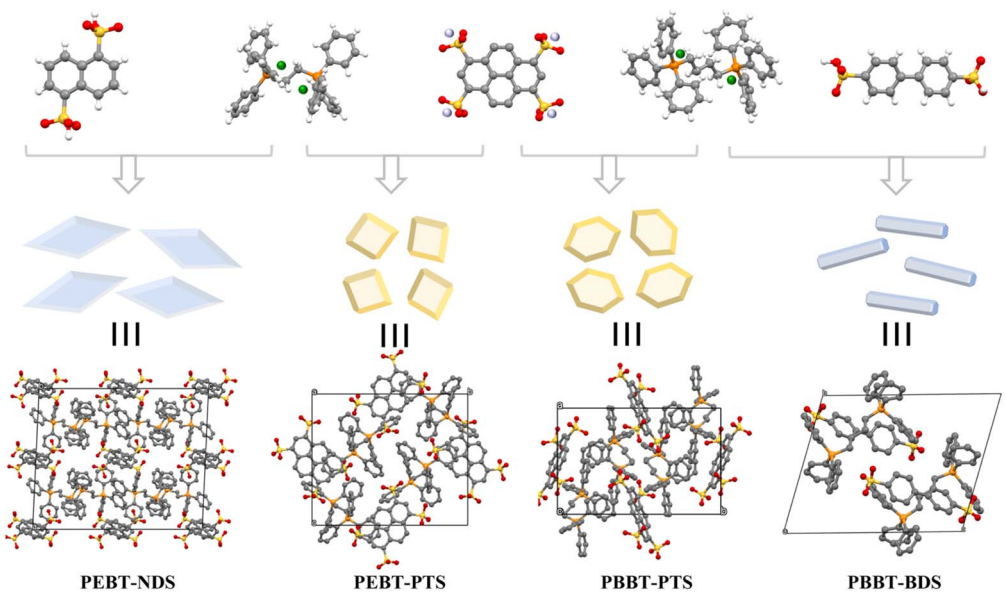

Scheme 1 Synthesis of four IOCs *via* pair-to-pair ionic self-assembly at room temperature in MeOH/H_2O.

Fig. 1a reveals that the NDS component in PEBT-NDS is arranged in four unique ways, while the PEBT moiety also exhibits four distinct arrangements, forming two sets of centrosymmetric configurations. PEBT-PTS (CCDC No. 2415290) is categorized under the monoclinic crystal system with a 2/*m* point group and a $P2_1/n$ space group. As depicted in Fig. 1b, PTS presents two different orientations, and the PEBT component maintains the same four arrangements with pairwise centrosymmetric construction as seen in PEBT-NDS. In addition, the crystal system, point group, and space group of PBBT-PTS (CCDC No. 2415291) and PEBT-PTS are consistent (Fig. 1c). In a similar vein to PEBT-NDS, PBBT-BDS (CCDC No. 2415292) is also a member of the triclinic crystal system, with a $\bar{1}$ point group and $P\bar{1}$ space group. Both the BDS and PBBT constituents in PBBT-BDS have two arrangements, as illustrated in Fig. 1d. A striking structural characteristic shared by these IOCs is their well-defined lamellar architecture, where alternating anionic and cationic layers create periodic electrostatic domains that govern both their structural and functional properties.

While PEBT-NDS and PEBT-PTS share identical phosphonium cations, their crystalline packing arrangements exhibit significant variations in cation conformation. This structural divergence becomes even more pronounced when comparing PBBT-BDS and PBBT-PTS. This difference can be attributed to the longer alkyl chain between the phosphorus atoms in PBBT, which allows for greater flexibility. This increased conformational freedom renders the phosphonium cations more responsive to anions, resulting in more pronounced lattice adaptations to accommodate different sulfonate anions. This is evidenced by the diverse angles of the benzene rings connected to phosphorus and the varying bending angles of the intermediate alkyl chain. As depicted in Fig. S1† and detailed in Table S3,† the plane angles of the benzene rings in PEBT for PEBT-NDS and PEBT-PTS are 63.04°, 69.35°, 87.68°, 57.90°, 66.29°, and 73.19° and 77.92°, 76.92°, 58.14°, 57.52°, 78.67°, and 63.55°, respectively, while for PBBT, they are 73.77°, 67.45°, 60.34°, 79.88°, 60.40°, and 79.18° (PBBT-BDS) and 84.42°, 83.72°, 60.75°, 50.98°, 85.26°, and 62.95° (PBBT-PTS). Fig. S2† illustrates the bond angles of the alkyl chain in PEBT for PEBT-NDS and PEBT-PTS as 114.23° and 113.92° and 113.54° and 112.05° and for PBBT as 117.96°, 113.14°, 111.07°, and 114.45° and 115.71°, 109.11°, 113.40°, and 113.86° in PBBT-NDS and PBBT-PTS, respectively. These data indicate that the two types of quaternary phosphonium salt cations are not entirely symmetrical, a characteristic that may arise from the influence of anions and the spatial constraints that cannot be ignored. Furthermore, Fig. S3† provides a topology diagram of the four IOCs, highlighting their structural differences. For ionic crystals,

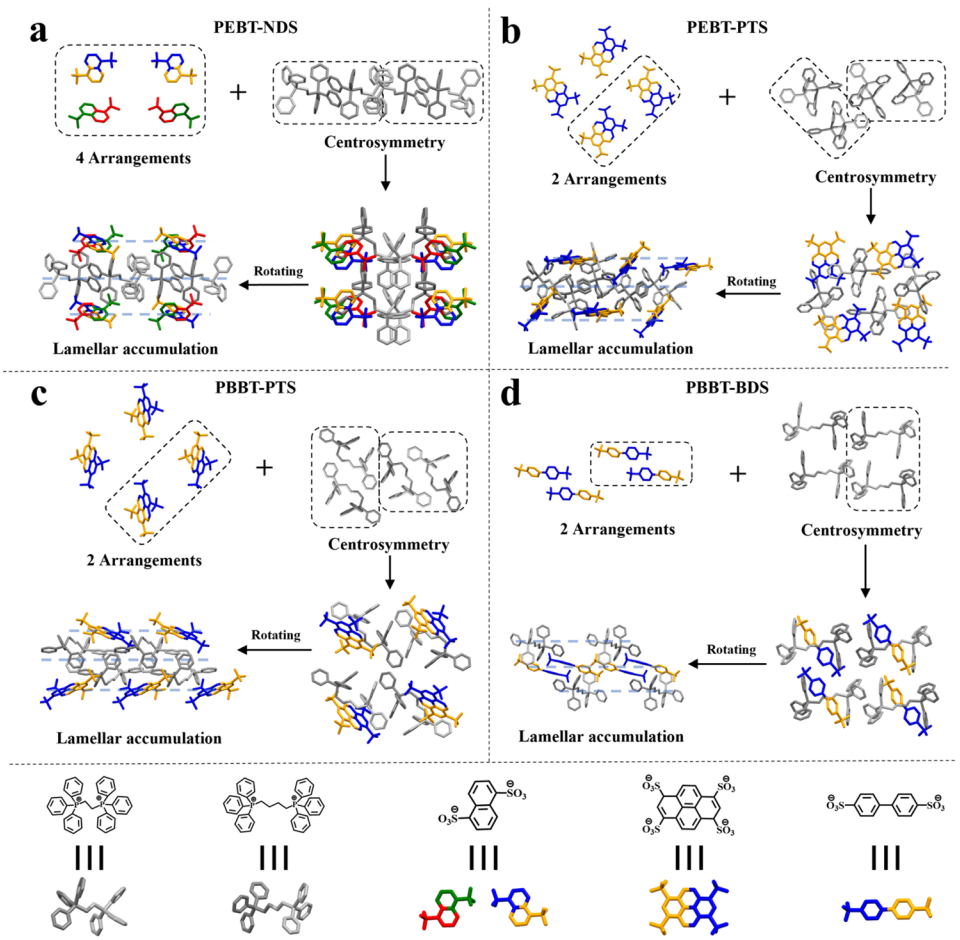

Fig. 1 Crystal structures of four IOCs of (a) PEBT-NDS, (b) PEBT-PTS, (c) PBBT-PTS and (d) PBBT-BDS.

the length of the ionic bond was one of the important indices to measure the strength of the ionic bond. As shown in Fig. S4,† the distances between P^+ in PEBT and O^- in NDS are 3.665 Å and 4.228 Å in PEBT-NDS. In the structure of PEBT-PTS, the distances between O^- on PTS and P^+ on adjacent PEBT are 3.801 Å, 3.801 Å, 4.029 Å, and 4.029 Å; the distances between the O^- on PTS and the P^+ on the adjacent PBBT are 4.279 Å, 4.279 Å, 4.419 Å, and 4.419 Å in PBBT-PTS; and the distances between O^- on BDS and P^+ on PBBT are 4.950 Å and 4.985 Å in PBBT-BDS, respectively. Crystallographic analysis revealed large interionic distances in IOCs, which can be attributed to the substantial steric demand of the phosphonium cations. This structural feature primarily stems from the combined effects of bulky triphenylphosphonium moieties creating significant spatial constraints and flexible alkyl bridges permitting adaptive lattice expansion.

Material characterization

Based on the provided information, it can be understood that the four IOCs exhibit relatively regular shapes under optical microscopy, such as PEBT-NDS appearing as rhombuses with diagonal lengths of 2495.6 μm and 966.8 μm (Fig. 2a); PEBT-PTS appearing as squares with sides approximately 1282.4 μm in length (Fig. 2b); PBBT-BDS appearing as rod-shaped crystals with a length of about 1718.0 μm (Fig. 2c); and PBBT-PTS appearing as hexagonal crystals with dimensions of 2099.2 μm in length and 1492.0 μm in width (Fig. 2d). XRD analysis of the single crystal powders for these four IOCs shows a high degree of consistency with the simulated XRD patterns, indicating high crystallinity and phase purity (Fig. 2e–h). Additionally, CO_2 adsorption–desorption tests reveal BET specific surface areas of 16.04 m g^{-1}, 10.18 m g^{-1}, 15.68 m g^{-1}, and 26.95 m g^{-1} for these materials, respectively, with the small surface areas suggesting a dense structure of these IOCs. The isothermal adsorption curves for PEBT-NDS, PEBT-PTS, and PBBT-PTS are similar, showing a sharp increase in adsorption capacity at low relative pressures, indicative of monolayer adsorption or chemical adsorption, followed by a transition to a multilayer adsorption or physical adsorption process as pressure increases. PBBT-BDS, on the other hand, shows a slight increase in adsorption capacity at low pressures, which

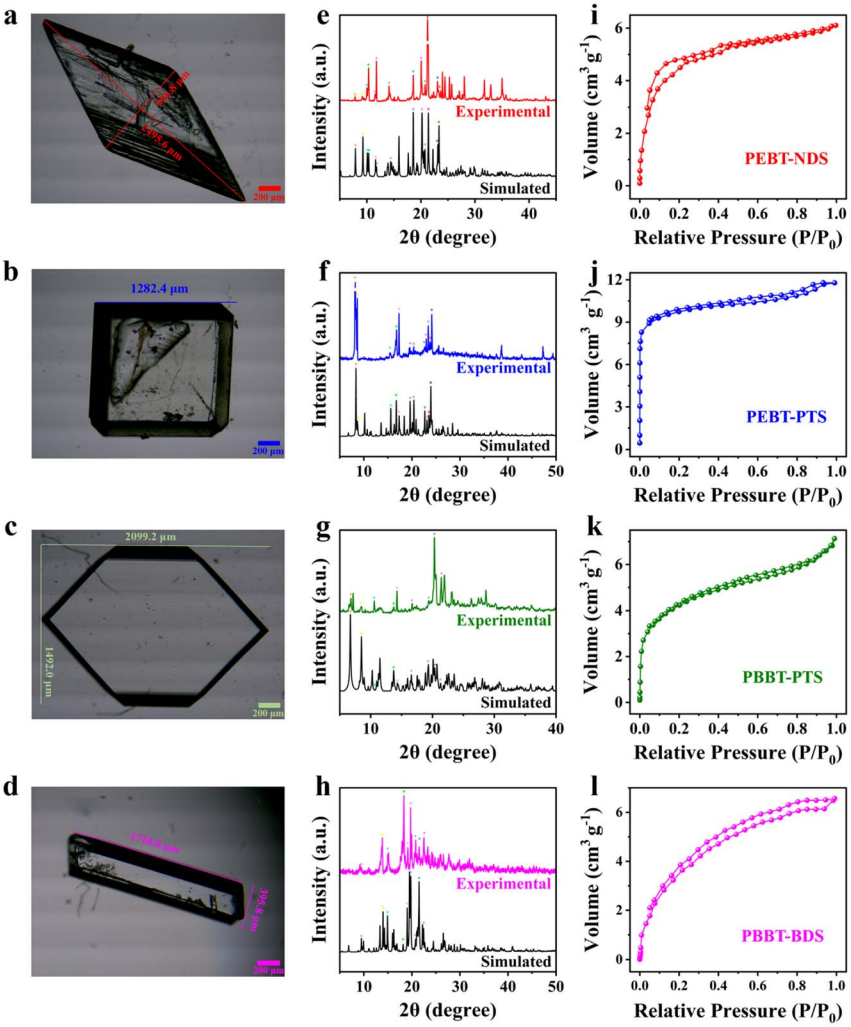

Fig. 2 Optical microscope photographs (a–d), XRD (e–h), and BET specific surface areas (i–l) of PEBT-NDS (a, e and i), PEBT-PTS (b, f and j), PBBT-PTS (c, g and k) and PBBT-BDS (d, h and l).

gradually intensifies with increasing pressure (Fig. 2i–l). TGA analysis demonstrates that these IOCs are thermally stable above 299 °C, providing a foundation for iodine adsorption experiments at high temperatures (Fig. S5†). Notably, the initial thermal weight loss temperature of single crystals using PBBT as the monomer is about 100 °C higher than those using PEBT as the monomer, indicating that the heat resistance of the material improved with the extension of the intermediate alkyl chain of the quaternary phosphonium monomer.

Adsorption performance of iodine in iodine–cyclohexane

Considering the molecular architecture of the four IOCs, which feature the incorporation of heteroatomic entities (phosphorus and sulfonic acid) alongside conjugated electron networks (benzene rings), it is anticipated that these materials will possess the ability to efficiently capture iodine. This is particularly relevant in the context of managing radioactive iodine, which is hazardous and challenging to control, especially in experimental settings involving the human body. Therefore, we utilized the non-radioactive isotope ^{127}I to simulate and study the adsorption of iodine in contaminated waste solutions.[10,45]

All iodine–cyclohexane solutions were analyzed using UV-Vis spectroscopy, with the absorbance at 525 nm serving as the quantitative benchmark. By measuring the absorbance of samples across different concentrations (0, 0.39, 0.78, 1.56, 3.13, 6.25, 12.5, 25, and 50 ppm), a correlation was established and a standard curve is presented in Fig. S6.† This curve was then utilized to quantify the unknown samples. The UV-Vis absorption curve in Fig. S7† was used to calculate the adsorption capacity at various times. Fig. S8† illustrates the iodine adsorption capabilities of the four materials in iodine-cyclohexane solutions of different concentrations (25 ppm and 50 ppm) over time. All four adsorbents exhibited comparable behavior, with rapid adsorption rates within the first 12 h. Subsequently, as the number of available active sites decreased, the adsorption rate slowed, reaching equilibrium in around 84 h, after which the adsorption amount remained relatively stable. The equilibrium adsorption capacities for iodine in cyclohexane solutions of PEBT-NDS, PEBT-PTS, PBBT-PTS, and PBBT-BDS were determined to be 22.9 mg g^{-1} (25 ppm) and 31.5 mg g^{-1} (50 ppm), 27.5 mg g^{-1} (25 ppm) and 34.4 mg g^{-1} (50 ppm), 23.5 mg g^{-1} (25 ppm) and 32.1 mg g^{-1} (50 ppm), and 23.5 mg g^{-1} (25 ppm) and 38.4 mg g^{-1} (50 ppm), respectively. Fig. S9† provides visual evidence of the change in color of the iodine–cyclohexane solution before and after adsorption, showing a marked lightening of the solution post-adsorption. The experimental data indicate that the adsorption of iodine in cyclohexane solutions by the four IOCs increases with the initial concentration, which can be attributed to the enhanced driving force for mass transfer at higher concentrations, thereby significantly improving the adsorption capacity. To further evaluate the iodine adsorption kinetics of the materials, pseudo-first-order and pseudo-second-order kinetic models were used to fit the experimental data. The results revealed that the four materials exhibit very similar degrees of fitting for both kinetic models, suggesting that the adsorption process is a mix of physical and chemical mechanisms. However, chemical adsorption predominantly governs the process, as evidenced by the slightly superior fitting degrees corresponding to the pseudo-second-order kinetic model. The details of the adsorption performance of iodine in iodine-cyclohexane are in the ESI.†

Adsorption performance of iodine vapor

Since radioactive iodine is sometimes released into air as a gas, in addition to examining the adsorption capacity of iodine in cyclohexane solution, this work also investigated the adsorption capacity of the material to iodine vapor. When exposed to iodine vapor at 70 °C (a temperature well below their thermal decomposition threshold of >299 °C, as evidenced by TGA), the four IOCs in 4 mL sample bottles progressively darkened from white/light yellow to black over time (Fig. S10†), directly visualizing iodine molecule adsorption. As illustrated in Fig. S11,† the adsorption equilibrium for the four crystals was achieved within 144 h for PEBT-NDS, 24 h for PEBT-PTS, 60 h for PBBT-PTS, and 36 h for PBBT-BDS, with maximum adsorption capacities of 1620 mg g^{-1}, 1430 mg g^{-1}, 1190 mg g^{-1}, and 590 mg g^{-1}, respectively. Notably, PBBT-BDS, which exhibited the least adsorption capacity, also displayed the lightest color, while PEBT-NDS, with the highest adsorption capacity, required the longest time to reach equilibrium. The analysis, which included BET measurements, indicated that despite PBBT-BDS having the largest specific surface area, its adsorption efficiency was inferior to that of the other three materials. This discrepancy suggests that adsorption is not only solely dependent on the specific surface area but is also influenced by the orientation of the functional group's active sites within the pores. Furthermore, the structural rigidity of anions may affect adsorption performance, as evidenced by the significantly reduced iodine capture capacity of the BDS-based material (exhibiting the lowest rigidity) compared to its other three rigid anion-derived counterparts. Then, the adsorption kinetics of the four adsorbents were analyzed and fitted. In line with the adsorption of iodine in iodine-cyclohexane, the adsorption of iodine vapor was also identified as a physical and chemical mixed adsorption process. However, in contrast to the previously mentioned chemical adsorption dominance, the adsorption of iodine vapor was primarily focused on physical adsorption. The details of the adsorption performance of iodine vapor are in the ESI.†

Release and retention of crystals after iodine vapor adsorption

The investigation focused on the iodine release characteristics of the four IOCs that had adsorbed iodine. The desorption process involved immersing the iodine-laden materials in cyclohexane and then heating them in an oven at a temperature of 70 °C to facilitate the release of iodine. Fig. 3 illustrates that the release rates are initially rapid within the first 2 h, subsequently slowing down and approaching a plateau. Notably, PEBT-NDS, PEBT-PTS, and PBBT-PTS exhibit swift release within 10 h (Fig. 3a–c), while PBBT-BDS demonstrates a more gradual release over approximately 36 h (Fig. 3d). The color change of the cyclohexane solution transitions from light to

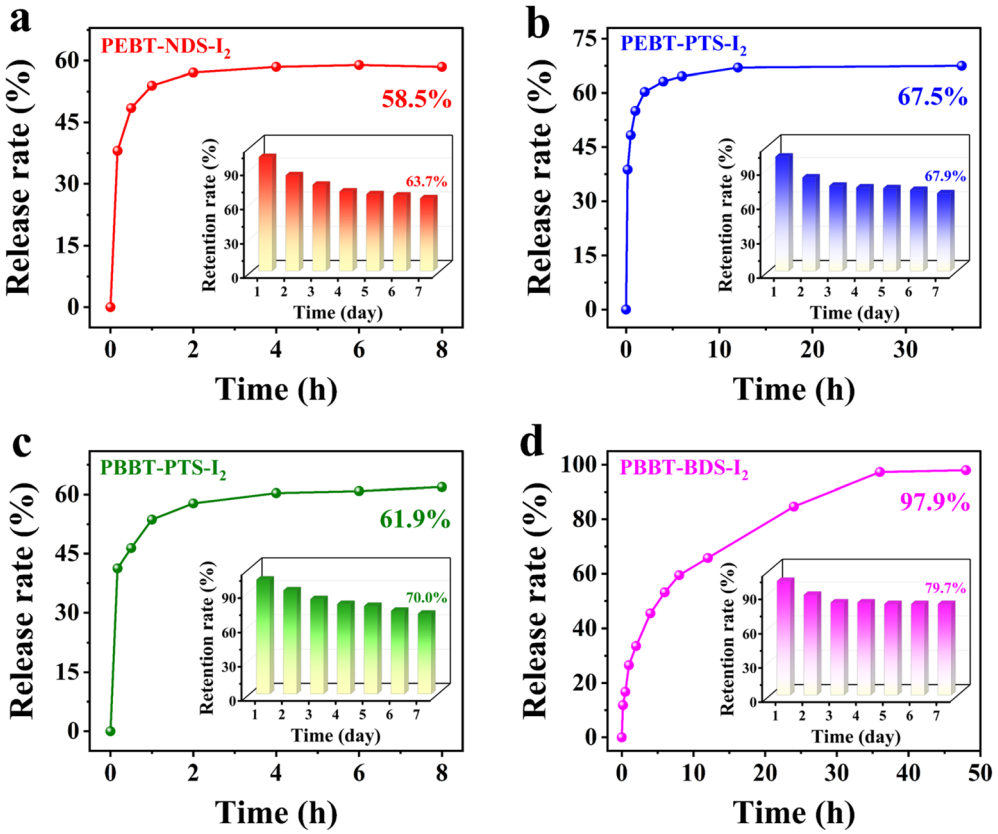

Fig. 3 The release rate of the four IOCs after iodine vapor adsorption with time at 70 °C and their corresponding retention rate at room temperature of (a) PEBT-NDS, (b) PEBT-PTS, (c) PBBT-PTS, and (d) PBBT-BDS.

dark, and conversely, the adsorbent at the bottom transitions from dark to a lighter shade, although still darker than the unused adsorbent (Fig. S12†). Upon reaching equilibrium, the iodine release efficiencies are 58.5% for PEBT-NDS-I_2, 67.5% for PEBT-PTS-I_2, 61.9% for PBBT-PTS-I_2, and 97.9% for PBBT-BDS-I_2, as indicated by the UV-Vis absorption curves in Fig. S13.† The high residual iodine content in the materials suggests that some iodine is chemically bonded within the material's pores, while the released iodine is physically adsorbed. This implies that iodine adsorption on PBBT-BDS is predominantly physical compared to that on the other three materials.

The iodine retention stability of adsorbents was systematically evaluated through time-dependent retention rate measurements (Fig. 3). All materials demonstrated sustained retention capabilities under ambient conditions, maintaining >63.7% iodine capture after 7 days. This extended retention performance holds dual significance for nuclear waste management: On the one hand, for long-lived ^{129}I, high retention capacity reduces leakage risks during geological storage, while for short-lived ^{131}I, effective retention during the first week ensures radiation intensity control throughout its critical decay period. The demonstrated retention properties satisfy the criteria for radioiodine containment systems through achieving an equilibrium between near-term radiological protection imperatives and longitudinal ecological security parameters. Furthermore, the solubility test of the four IOCs demonstrates remarkably complete dissolution in DMSO (Table S4 and Fig. S14†), confirming that the non-crosslinked architectures effectively avoid the solvation barriers typically imposed by rigid polymeric frameworks. This structural advantage not only facilitates rapid iodine release kinetics but also crucially enables exceptional solution processability.[46]

Adsorption mechanism

To delve deeper into the chemical state of iodine on the materials' surfaces and to investigate the interactions between the adsorbents and iodine, a comprehensive series of analytical techniques including TGA, XPS, FT-IR, Raman Spectroscopy, and EDS was employed to characterize the four crystals before and after iodine adsorption. Fig. S15† presents the TGA data for the materials, illustrating that the weight loss observed in the adsorbed materials prior to reaching the decomposition point is attributed to the release of iodine. The percentage of iodine released as determined by thermogravimetry was 64.5% for PEBT-NDS-I_2, 52.8% for PEBT-PTS-I_2, 38.7% for PBBT-PTS-I_2, and 96.6% for PBBT-BDS-I_2, respectively. Notably, the release rates of PEBT-NDS-I_2 and PBBT-BDS-I_2 from thermogravimetry are in close agreement with those observed when the adsorbed materials were soaked in cyclohexane (58.5% for PEBT-NDS-I_2 and 97.9% for PBBT-BDS-I_2). However, the release rates of PEBT-PTS-I_2 and PBBT-PTS-I_2 from thermogravimetry are lower compared to those in cyclohexane (67.5% for PEBT-PTS-I_2 and

61.9% for PBBT-PTS-I_2, as seen in Fig. 3). This discrepancy may arise because PEBT-PTS-I_2 and PBBT-PTS-I_2 release I_3^- through chemical adsorption in cyclohexane, and the limited solubility of I_3^- in cyclohexane leads to its conversion to I_2, thereby resulting in higher measured release rates. This conclusion is further supported by Fig. S16,† which indicates the presence of I_3^- peaks (at around 280 and 350 nm) during the release process of PEBT-PTS-I_2 and PBBT-PTS-I_2.

To further validate the form of iodine present in the adsorbents, XPS was utilized to characterize the materials before and after iodine adsorption. As depicted in Fig. 4a–d, the appearance of new I 3d and I 4d peaks in the full spectrum of all four materials post-adsorption confirms the presence of iodine. Through peak fitting of the I 3d high-resolution spectrum, distinct peaks for I_2, I_3^-, and I_5^- were observed at around 630 eV and 620 eV, signifying that these three iodine species have been effectively adsorbed onto the materials' surfaces.[47,48] Fig. S17† illustrates that the high-resolution spectra of S and O have experienced a shift following adsorption. Notably, the displacement change for PBBT-BDS is the least significant, which may correlate with a predominantly physical adsorption mechanism for this material. In contrast, the other three materials exhibit a greater degree of chemical adsorption. Additionally, the binding energy of phosphorus (P) remains largely unchanged, suggesting that P may have a minimal role in the adsorption process. This observation is likely connected to the fact that all of phosphorus's electrons and orbitals are already engaged in bonding within the crystal structure. As observed in Fig. S18,† the π–π* conjugate peaks of PEBT-NDS and PEBT-PTS, which have higher adsorption capacities, decreased substantially after iodine adsorption. This reduction indicates that the benzene ring within these materials is also involved in the iodine adsorption process.[46,49] The XPS spectra thus confirm the formation of charge transfer complexes (I_3^- and I_5^-) during the adsorption of iodine. Furthermore, S, O and the benzene ring within the crystal structures emerge as the primary adsorption sites, highlighting their significant role in the adsorption mechanism.

Additionally, the FT-IR spectra depicted in Fig. 5a–d reveal that the characteristic peaks of the materials remain largely consistent before and after iodine adsorption, indicating that the fundamental structure of the materials' network remains intact. Nevertheless, notable shifts in certain peak positions are observed. Following the adsorption of iodine vapor, the sulfonic acid peaks, typically found in the range of 1200–1000 cm^{-1}, and the phenyl peaks at around 1439 cm^{-1} for all four materials exhibit displacement, which is indicative of chemisorption processes.[50,51]

After that, Raman spectroscopy of the materials confirms the presence of iodine in various forms, including I_2, I_3^-, and I_5^-.[20] Notably, the PBBT-BDS material exhibits a significantly higher content of I_2 compared to the other three materials, as evidenced in Fig. 5e–h. This finding corresponds with the data from the iodine release experiment, TGA (Fig. S15), and XPS (Fig. S17†).

Then, EDS and element distribution mapping, as shown in Tables S5, S6, Fig. S19 and S20,† reveal a marked presence of iodine elements in the adsorbent materials after adsorption, with an even distribution across the surface. Additionally, the iodine content from Table S6† in PBBT-BDS-I_2 (2.15%) is significantly lower than that found in the other materials (6.15%, 6.18%, and 6.27%). These results suggest that the primary adsorption sites for iodine within the material network are likely the sulfonic acid groups and the benzene rings, with iodine being adsorbed in the forms of I_2, I_3^-, and I_5^-.

Lastly, the accurate determination of the binding site of iodine on a single crystal is of great significance for understanding the adsorption mechanism and designing iodine capture separation materials in the future. Consequently, utilizing PEBT-NDS, which exhibits superior adsorption

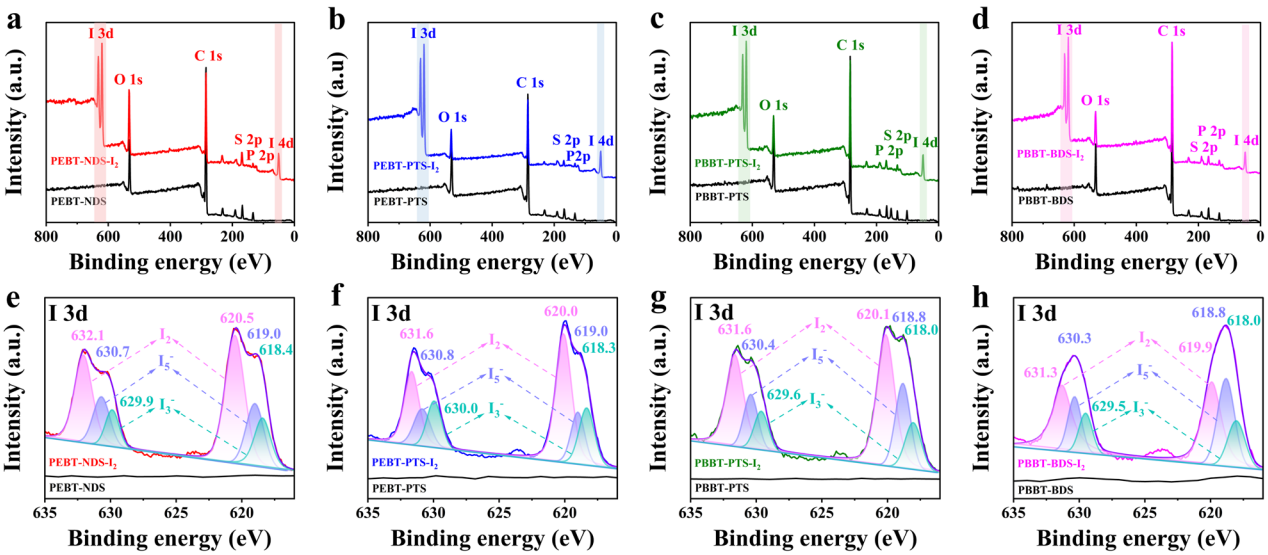

Fig. 4 The XPS full spectrum of the four IOCs before and after iodine adsorption of (a) PEBT-NDS, (b) PEBT-PTS, (c) PBBT-PTS, and (d) PBBT-BDS and the corresponding I 3d high-resolution spectrum (e–h).

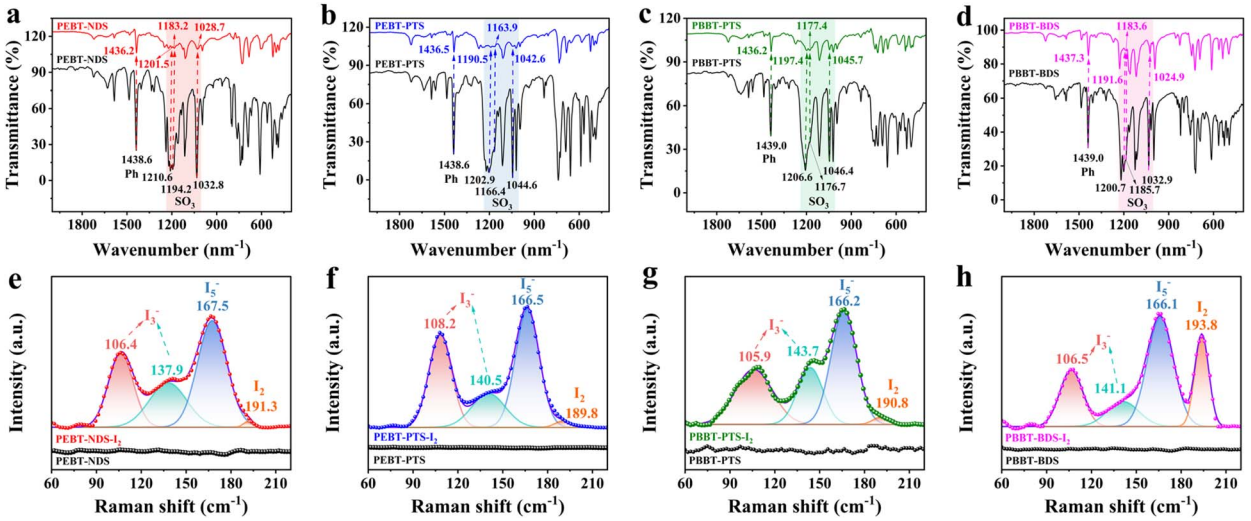

Fig. 5 FT-IR spectrum of the four IOCs before and after iodine adsorption of (a) PEBT-NDS, (b) PEBT-PTS, (c) PBBT-PTS, and (d) PBBT-BDS and the corresponding Raman spectrum (e–h).

efficacy, as a case study, density functional theory (DFT) calculations were employed to delve into the iodine capture by the material. Drawing on the XPS, FT-IR, and Raman spectroscopy findings presented earlier, we consider the iodine species to be I_2, I_3^-, and I_5^-, with the sulfonic acid and benzene ring serving as the primary adsorption sites. Thus, the investigation was focused on determining the lowest energy configuration for the iodine adsorption system involving the benzene ring and sulfonic acid groups. Among the various configurations examined, the lowest configurations corresponding to I_2, I_3^-, and I_5^- are O (of sulfonic acid)-I_2, ring 1 (of PEBT)-I_3^-, and ring 1 (of PEBT)-I_5^-, respectively. For I_2 adsorption on the sulfonic acid group (O site), the adsorption energy (−0.60 eV) and short distance (2.64 Å) indicate physical adsorption dominated by electrostatic interactions between the negatively charged O atom and polarizable I_2. In contrast, the benzene ring exhibits stronger chemical interactions with polyiodides: I_3^- and I_5^- bind with adsorption energies of −1.36 eV and −1.39 eV at distances of 3.50 Å and 3.51 Å, respectively, driven by π-electron donation from the aromatic system. This indicates the synergistic roles of functional groups-sulfonic acid anchors I_2 physically, while the benzene ring chemically stabilizes polyiodides through π-interactions. This dual functionality highlights the material's potential for tailored iodine capture, where optimizing functional group spatial arrangement could enhance selectivity toward specific iodine species. The adsorption energies for the other systems are also negative, ranging from −0.42 to −0.83 eV, indicating that the adsorption processes are thermodynamically favorable. The distances between the active sites and the iodine atoms vary from 2.51 Å to 3.57 Å, as illustrated in Fig. S21,† and the interatomic distances within the iodine molecules and polyiodide anion range between 2.69 Å and 3.74 Å, as detailed in Table S7.† As shown in Fig. S22,† the charge transfer range of the system is from −0.45 *e* to 0.02 *e*. This indicates that electrons accumulate near iodide ions, and iodine mainly acts as an electron acceptor during the adsorption process.[52,53]

According to the charge potential energy model, when an atom forms a bond with others, if the density of the outer-shell electron cloud decreases (for example, electrons are attracted by other atoms), the positively charged atomic nucleus will have an increased attraction for the remaining inner-shell electrons, leading to an increase in the binding energy of the inner-shell electrons. Combined with high-resolution S 2p XPS spectra and O 1s XPS spectra before and after iodine adsorption (Fig. S17a–c†), the S 2p binding energy of PEBT-NDS shifted from 167.0 and 168.2 eV to 168.3 and 169.3 eV after iodine adsorption, indicating a decrease in outer-shell electron cloud density around sulfur atoms due to electron donation to iodine species. Similarly, the O 1s peak shifted from 530.6 and 531.5 eV to 531.3 eV to 532.7 eV, consistent with the sulfonic acid group acting as an electron donor. These shifts align quantitatively with the DFT-calculated charge transfer values: in the O–I_2 system (charge transfer = −0.13 *e*), the sulfonic acid oxygen donates electrons to I_2, leading to the observed O 1s binding energy increase. For ring 1-I_5^- (charge transfer = −0.45 *e*), the significant electron depletion on the benzene ring correlates with the attenuation of the π–π* satellite peak in the C 1s spectrum (Fig. S18a†), confirming the π-electron participation in iodine chemisorption. This direct correspondence between DFT-derived charge transfer and experimental XPS shifts robustly supports the proposed mixed adsorption mechanism.

Collectively, the DFT calculations demonstrate that IOCs cooperatively drive iodine adsorption through electrostatic anchoring by the sulfonic acid groups and π-mediated stabilization by the benzene rings. These synergistic interactions facilitate the formation of polyiodoanion complexes as directly visualized in the charge transfer dynamics and structural evolution depicted in Fig. 6g. A detailed account of the calculations can be found in the ESI.†

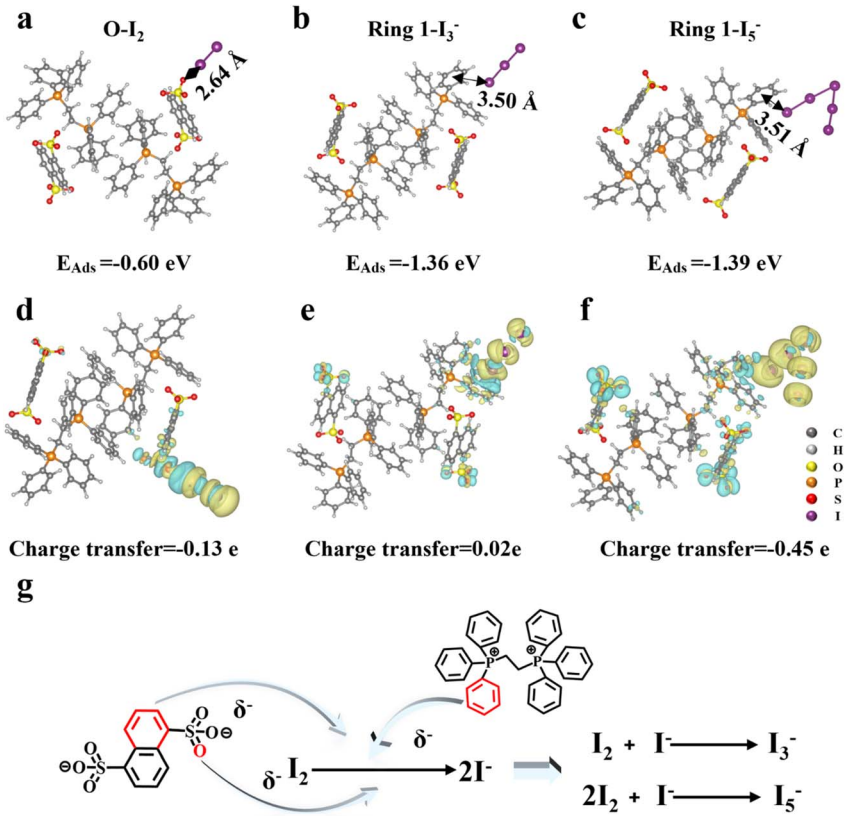

Fig. 6 Adsorption energies and distances of (a) O–I_2, (b) ring 1-I_3^-, and (c) ring 1-I_5^-, and corresponding charge transfer diagrams (d–f), and (g) formation mechanism of polyiodide anions.

Comparison with other adsorbents

The adsorbents with the best adsorption capacity in this work were compared with those reported in the literature, as shown in Table S8.† The maximum iodine adsorption capacity of adsorbents (PEBT-NDS) is on par with that of COF-TpgBD,[54] NACs-TPAPyH,[55] and UiO-66-NH-TD,[56] and it surpasses the capacities of Etp6β[46] and COFs@cotton.[57] However, its capacity is less than that of BPy-Cage,[10] BPy-Box·4Cl,[58] TJNU-203,[59] and SCU-SnS.[60] Regarding the adsorption temperature, PEBT-NDS operates at the same temperature as NACs-TPAPyH,[55] which is lower than the temperatures required for the other materials listed. This suggests that PEBT-NDS can adsorb iodine efficiently at a lower temperature, which is an advantage in terms of energy consumption and operational costs. The adsorption time for PEBT-NDS is similar to that of TJNU-203 (ref. 59) and SCU-SnS,[60] indicating a longer duration of adsorption when compared to the other adsorbent materials. This prolonged adsorption time can be beneficial in applications where stability and long-term retention of iodine are critical. Whether the synthesis conditions are mild and environmentally friendly is also an important aspect for testing the significance of materials. The IOCs introduced in this article can all be synthesized at room temperature within 12 h, which saves energy. Like IOCs, BPy-Cage Etp6β was also synthesized at room temperature for 12 h. In addition, NACs-TPAPyH[55] and COFs@cotton[57] were synthesized at room temperature, while the rest of the materials were synthesized at low temperature (COF-TpgBD[54]) or high temperature (UiO-66-NH-TD,[56] BPy-Box·4Cl,[58] TJNU-203 (ref. 59) and SCU-SnS[60]) for a time longer than 12 h.

Collectively, PEBT-NDS exhibits exceptional iodine adsorption capacity (1620 mg g^{-1}), operates effectively under lower-temperature conditions (25 °C), and demonstrates sustained adsorption performance over extended operational periods (144 h), while maintaining energy efficiency and environmental compatibility. These synergistic characteristics position this material as a promising candidate for advanced nuclear waste management systems requiring high-performance iodine capture and sequestration.

Conclusion and prospects

In conclusion, four different IOCs named PEBT-NDS, PEBT-PTS, PBBT-PTS, and PBBT-BDS were first prepared with two phosphonium cationic monomers and three sulfonyl anionic monomers *via* pair-to-pair ionic self-assembly. Then their physical and chemical properties were characterized by using an X-ray single crystal diffractometer, optical microscopy, XRD, TGA, and BET. The IOCs were evaluated as adsorbents for iodine, demonstrating adsorption capacities ranging from 22.9 to 27.5 mg g^{-1} in iodine–cyclohexane solutions at 25 ppm and from 31.5 to 38.4 mg g^{-1} at 50 ppm. In addition, their iodine vapor adsorption capacity reached up to 590 mg g^{-1} to 1620 mg g^{-1}. Through kinetic fitting, it was proved that the adsorption of iodine in both iodine–cyclohexane solution and in the vapor

adsorption process belongs to the physical and chemical mixed adsorption mode. Investigations into the release of adsorbed iodine revealed that complete release was not achievable for any of the four materials, indicating that while some iodine was adsorbed physically and could be released relatively easily, a significant portion was adsorbed chemically in the form of polyiodide anions, which were more difficult to desorb. Notably, PEBT-PTS exhibited a higher physical adsorption ratio, which may be attributed to the specific arrangement of adsorption sites within the material. To elucidate the adsorption mechanisms of the IOCs, further analyses and calculations were conducted using TGA, FT-IR, XPS, Raman spectroscopy, EDS, and DFT. These analyses confirmed the presence of iodine in the forms of I_2, I_3^-, and I_5^-, reinforcing the conclusion that the adsorption process was a mixed physical and chemical adsorption. In a word, this paper for the first time proposed a method to prepare quaternary phosphonium-based IOCs by self-assembly under mild conditions, which can be used for iodine adsorption.

The success of phosphonium–sulfonate IOCs in iodine capture opens avenues for further exploration. Firstly, this ion self-assembly strategy can be extended from N-base sites such as imidazole and pyridine to quaternary phosphonium cation–anion pairs, and it provides a model for the self-assembly of other ion pairs (such as guanidine, carboxylic, phosphate, and diazo groups). Secondly, structural optimization of existing IOCs-such as modulating alkyl chain flexibility, introducing electron-deficient aromatic units, or increasing sulfonate group density-may improve adsorption capacity and chemical stability under harsh conditions (*e.g.*, high humidity or radiation). Thirdly, scaling up the synthesis process while maintaining crystallinity and exploring recyclability are critical steps toward practical applications. Additionally, beyond iodine adsorption, these IOCs have potential in environmental remediation, energy storage, gas separation, catalysis, and sensors due to their structural flexibility and functional groups. Finally, integrating machine learning with high-throughput DFT calculations could accelerate the design of next-generation IOCs with programmable adsorption functionalities.

Data availability

All the relevant data of this study are available within the manuscript and its ESI.†

Author contributions

Jia Chen and Hongdeng Qiu did the conceptualization, funding acquisition, and writing-review & editing, Mingxia Sun did investigation, carried out the methodology, and wrote the original draft, Ting Zhang and Wei Xu did the validation and data curation, Jing He and Yunyun Zhang did the software analysis, Huifeng Liu and Shuang Zhang did the visualisation, Juanjuan Wang, Xin Li, and Yali Yang did the software analysis. All authors contributed to discussions regarding the results and the manuscript.

Conflicts of interest

There are no conflicts to declare.

Acknowledgements

This work was supported by the National Natural Science Foundation of China (No. 22374159 and 22474141), the Gansu Province Outstanding Youth Fund project (24JRRA042), and the Youth Innovation Promotion Association CAS (2021420).

Notes and references

1 M. Goswami, M. Toro-González, J. Moon and S. Davern, Precision atomistic structures of actinium-/radium-/barium-doped lanthanide nanoconstructs for radiotherapeutic applications, *ACS Nano*, 2024, **18**, 16577–16588.
2 D. Sarma, C. D. Malliakas, K. S. Subrahmanyam, S. M. Islam and M. G. Kanatzidis, $K_{2x}Sn_{4-x}S_{8-x}$ (x=0.65-1): A new metal sulfide for rapid and selective removal of Cs^+, Sr^{2+} and UO_2^{2+} ions, *Chem. Sci.*, 2015, **7**, 1121–1132.
3 M. E. Simms, Z. Li, M. M. Sibley, A. S. Ivanov, C. M. Lara, T. C. Johnstone, V. Kertesz, A. Fears, F. D. White, D. L. J. Thorek and N. A. Thiele, PYTA: a universal chelator for advancing the theranostic palette of nuclear medicine, *Chem. Sci.*, 2024, 11279–11286.
4 M. Yang, F. Qiu, E.-S. M El-Sayed, W. Wang, S. Du, K. Su and D. Yuan, Water-stable hydrazone-linked porous organic cages, *Chem. Sci.*, 2021, **12**, 13307–13315.
5 P. Lappi and J. Lintunen, From cradle to grave? On optimal nuclear waste disposal, *Energy Econ.*, 2021, **103**, 5556.
6 M. Nyman and G. Deblonde, Metal-oxide cage traps radioactive element, *Nature*, 2023, **616**, 438–440.
7 Q. Guo, J. Li, Y. Zhao, L. Li, L. He, F. Zhao, F. Zhai, M. Zhang, L. Chen, Z. Chai and S. Wang, Record high iodate anion capture by a redox-active cationic polymer network, *Angew. Chem., Int. Ed.*, 2024, **63**, e202400849.
8 J. E. Ten Hoeve and M. Z. Jacobson, Worldwide health effects of the Fukushima Daiichi nuclear accident, *Energy Environ. Sci.*, 2012, **5**, 8743–8757.
9 A. Saiz-Lopez, J. M. C. Plane, A. R. Baker, L. J. Carpenter, R. von Glasow, J. C. G. Martin, G. McFiggans and R. W. Saunders, Atmospheric chemistry of iodine, *Chem. Rev.*, 2012, **112**, 1773–1804.
10 D. Luo, Y. He, J. Tian, J. L. Sessler and X. Chi, Reversible iodine capture by nonporous adaptive crystals of a bipyridine cage, *Nat. Commun.*, 2022, **144**, 113–117.
11 A. J. Juhola, Iodine adsorption and structure of activated carbons, *Carbon*, 1975, **13**, 437–442.
12 C. Zhao, L. Ge, M. Zuo, L. Mai, S. Chen, X. Li, Q. Li, Y. Wang and C. Xu, Study on the mechanical strength and iodine adsorption behavior of coal-based activated carbon based on orthogonal experiments, *Energy*, 2023, **282**, 128450.
13 X. Zhang, P. Gu, X. Li and G. Zhang, Efficient adsorption of radioactive iodide ion from simulated wastewater by nano

Cu_2O/Cu modified activated carbon, *Chem. Eng. J.*, 2017, **322**, 129–139.

14 B. Liu, X. Ren, L. Chen, X. Ma, Q. Chen, Q. Sun, L. Zhang, P. Si and L. Ci, High efficient adsorption and storage of iodine on S, N co-doped graphene aerogel, *J. Hazard. Mater.*, 2019, **373**, 705–715.

15 S. M. Scott, T. Hu, T. Yao, G. Xin and J. Lian, Graphene-based sorbents for iodine-129 capture and sequestration, *Carbon*, 2015, **90**, 1–8.

16 X. Zhang, J. Maddock, T. M. Nenoff, M. A. Denecke, S. Yang and M. Schroder, Adsorption of iodine in metal-organic framework materials, *Chem. Soc. Rev.*, 2022, **51**, 3243–3262.

17 X. Zhang, I. da Silva, H. G. W. Godfrey, S. K. Callear, S. A. Sapchenko, Y. Cheng, I. Vitorica-Yrezabal, M. D. Frogley, G. Cinque, C. C. Tang, C. Giacobbe, C. Dejoie, S. Rudic, A. J. Ramirez-Cuesta, M. A. Denecke, S. Yang and M. Schroder, Confinement of iodine molecules into triple-helical chains within robust metal-organic frameworks, *J. Am. Chem. Soc.*, 2017, **139**, 16289–16296.

18 Y. Lei, G. Zhang, Q. Zhang, L. Yu, H. Li, H. Yu and Y. He, Visualization of gaseous iodine adsorption on single zeolitic imidazolate framework-90 particles, *Nat. Commun.*, 2021, **12**, 4483.

19 D. F. Sava, M. A. Rodriguez, K. W. Chapman, P. J. Chupas, J. A. Greathouse, P. S. Crozier and T. M. Nenoff, Capture of volatile iodine, a gaseous fission product, by zeolitic imidazolate framework-8, *J. Am. Chem. Soc.*, 2011, **133**, 12398–12401.

20 Y. Xie, T. Pan, Q. Lei, C. Chen, X. Dong, Y. Yuan, W. Al Maksoud, L. Zhao, L. Cavallo, I. Pinnau and Y. Han, Efficient and simultaneous capture of iodine and methyl iodide achieved by a covalent organic framework, *Nat. Commun.*, 2022, **13**, 2878.

21 X. Yan, Y. Yang, G. Li, J. Zhang, Y. He, R. Wang, Z. Lin and Z. Cai, Thiophene-based covalent organic frameworks for highly efficient iodine capture, *Chin. Chem. Lett.*, 2023, **34**, 107201.

22 J. Chang, H. Li, J. Zhao, X. Guan, C. Li, G. Yu, V. Valtchev, Y. Yan, S. Qiu and Q. Fang, Tetrathiafulvalene-based covalent organic frameworks for ultrahigh iodine capture, *Chem. Sci.*, 2021, **12**, 8452–8457.

23 N. Arora, T. Debnath, M. C. Senarathna, R. M. Johnson, I. G. Roske, G. A. Cisneros and R. A. Smaldone, Rapid, high-capacity adsorption of iodine from aqueous environments with amide functionalized covalent organic frameworks, *Chem. Sci.*, 2024, **15**, 3571–3577.

24 L. He, L. Chen, X. Dong, S. Zhang, M. Zhang, X. Dai, X. Liu, P. Lin, K. Li, C. Chen, T. Pan, F. Ma, J. Chen, M. Yuan, Y. Zhang, L. Chen, R. Zhou, Y. Han, Z. Chai and S. Wang, A nitrogen-rich covalent organic framework for simultaneous dynamic capture of iodine and methyl iodide, *Chem*, 2021, **7**, 699–714.

25 Z.-W. Li, Z.-J. Huang, Y.-X. Li, X. Wu, W. Shi, Y.-B. Zhang, X. Ma, G. Ouyang, B.-H. Ye, G.-F. Liu and X.-M. Chen, An ultrastable, easily scalable and regenerable macrocycle-based hydrogen-bonded organic framework, *CCS Chem.*, 2025, **7**, 293–306.

26 L. Lin, H. Guan, D. Zou, Z. Dong, Z. Liu, F. Xu, Z. Xie and Y. Li, A pharmaceutical hydrogen-bonded covalent organic polymer for enrichment of volatile iodine, *RSC Adv.*, 2017, **7**, 54407–54415.

27 B. Li, W. Qiu, G. P. A. Yap, Y. L. Dory and J. P. Claverie, Hydrogen-bonded organic frameworks based on endless-stacked amides for iodine capture and detection, *Adv. Funct. Mater.*, 2023, **34**, 2311964.

28 Z. Yan, Y. Yuan, Y. Tian, D. Zhang and G. Zhu, Highly efficient enrichment of volatile iodine by charged porous aromatic frameworks with three sorption sites, *Angew. Chem., Int. Ed.*, 2015, **54**, 12733–12737.

29 Y. Lin, X. Jiang, S. T. Kim, S. B. Alahakoon, X. Hou, Z. Zhang, C. M. Thompson, R. A. Smaldone and C. Ke, An elastic hydrogen-bonded cross-linked organic framework for effective iodine capture in water, *J. Am. Chem. Soc.*, 2017, **139**, 7172–7175.

30 D. Dai, J. Yang, Y.-C. Zou, J.-R. Wu, L.-L. Tan, Y. Wang, B. Li, T. Lu, B. Wang and Y.-W. Yang, Macrocyclic arenes-based conjugated macrocycle polymers for highly selective CO_2 capture and iodine adsorption, *Angew. Chem., Int. Ed.*, 2021, **60**, 8967–8975.

31 M. Zhang, J. Samanta, B. A. Atterberry, R. Staples, A. J. Rossini and C. Ke, A crosslinked ionic organic framework for efficient iodine and iodide remediation in water, *Angew. Chem., Int. Ed.*, 2022, **61**, e202214189.

32 L. Xie, Z. Zheng, Q. Lin, H. Zhou, X. Ji, J. L. Sessler and H. Wang, Calix 4 pyrrole-based crosslinked polymer networks for highly effective iodine adsorption from water, *Angew. Chem., Int. Ed.*, 2022, **61**, e202113724.

33 C. Liu, Y. Jin, Z. Yu, L. Gong, H. Wang, B. Yu, W. Zhang and J. Jiang, Transformation of porous organic cages and covalent organic frameworks with efficient iodine vapor capture performance, *J. Am. Chem. Soc.*, 2022, **144**, 12390–12399.

34 X. Cao, Y. Jin, H. Wang, X. Ding, X. Liu, B. Yu, X. Zhan and J. Jiang, A tetraaldehyde-derived porous organic cage and covalent organic frameworks: Syntheses, structures, and iodine vapor capture, *Chin. Chem. Lett.*, 2024, **35**, 109201.

35 C. Liu, Y. Jin, Z. Yu, L. Gong, H. Wang, B. Yu, W. Zhang and J. Jiang, Transformation of porous organic cages and covalent crganic frameworks with efficient iodine vapor capture performance, *J. Am. Chem. Soc.*, 2022, **144**, 12390–12399.

36 M. Wathier and M. W. Grinstaff, Synthesis and properties of supramolecular ionic networks, *J. Am. Chem. Soc.*, 2008, **130**, 9648–9649.

37 S. L. Craig, From ionic liquids to supramolecular polymers, *Angew. Chem., Int. Ed.*, 2009, **48**, 2645–2647.

38 J.-B. Ming, X. Li, J. Li, W. Yu and W. Wang, Organic molecule-ionic solids of structurally mismatched ion pairs formed via attractive interactions, *Cryst. Growth Des.*, 2022, **22**, 1212–1220.

39 H. Liu, Y. He, J. Chen, X. Qu, J. He, X. Chen, J. Wang and H. Qiu, Chiral ionic organic single-crystal and its exfoliated

two-dimensional nanosheets with enhanced enantioseparation, *Chem. Sci.*, 2024, **15**, 18818.

40 Y. Zhang, J. Chen, Q. He, J. He, W. Xu, M. Sun and H. Qiu, Selective separation of thorium from rare earth ions using bisphosphonate-functionalized ionic single crystals co-self-assembled via π–π and ionic interactions, *Nano Lett.*, 2025, **25**, 7665–7672.

41 W. Xu, C. Gao, Y. Zhang, M. Sun, H. Qiu and J. Chen, Ionic self-assembled single-crystal for highly efficient capture of iodine, *Sep. Purif. Technol.*, 2025, **364**, 132495.

42 R. Li, X. Tang, J. Wu, K. Zhang, Q. Zhang, J. Wang, J. Zheng, S. Zheng, J. Fan, W. Zhang, X. Li and S. Cai, A sulfonate-functionalized covalent organic framework for record-high adsorption and effective separation of organic dyes, *Chem. Eng. J.*, 2023, **464**, 142706.

43 S. Lin, M. Su, X. Li and S.-x. Liang, Solvent-free mechanochemical synthesis of a sodium disulfonate covalent organic framework for simultaneous highly efficient selective capture and sensitive fluorescence detection of fluoroquinolones, *Sep. Purif. Technol.*, 2024, **336**, 126167.

44 Y. Liu, Y. Zhu, Q. Mao and W. Chen, Enhanced hydrophilicity of DAAQ-TFP COFs via sulfonate modification for air water harvesting in arid environment, *Small*, 2024, **20**, 2406803.

45 S. Sun, X. Sha, J. Liang, G. Yang, X. Hu, Z. He, M. Liu, N. Zhou, X. Zhang and Y. Wei, Rapid synthesis of polyimidazole functionalized MXene via microwave-irradiation assisted multi-component reaction and its iodine adsorption performance, *J. Hazard. Mater.*, 2021, **420**, 126580.

46 K. Jie, Y. Zhou, E. Li, Z. Li, R. Zhao and F. Huang, Reversible iodine capture by nonporous pillar 6 arene crystals, *J. Am. Chem. Soc.*, 2017, **139**, 15320–15323.

47 X. Gao, Q.-H. Hu, Y.-Z. Shi, R.-P. Liang and J.-D. Qiu, Rationally designing imidazole-based coordination polymers with high adsorption capacity for removing iodine, *Chem. Eng. J.*, 2023, **468**, 130578.

48 K. Cheng, H. Li, J. R. Wang, P. Z. Li and Y. Zhao, From supramolecular organic cages to porous covalent organic frameworks for enhancing iodine adsorption capability by fully exposed nitrogen-rich sites, *Small*, 2023, **19**, e2301998.

49 N. Arora, T. Debnath, M. C. Senarathna, R. M. Johnson, I. G. Roske, G. A. Cisneros and R. A. Smaldone, Rapid, high-capacity adsorption of iodine from aqueous environments with amide functionalized covalent organic frameworks, *Chem. Sci.*, 2024, **15**, 3571–3577.

50 S.-N. Liu, H.-N. Wang, M.-L. Feng, K.-L. Yang, S. Cai, J. Fan, W.-G. Zhang and S.-R. Zheng, Metal-organic cage extended amorphous network via anionic organic linkers for $Cr_2O_7^{2-}$ and iodine adsorption on nanopores, *ACS Appl. Nano Mater.*, 2022, **6**, 656–663.

51 N. M. Shishlov and S. L. Khursan, Effect of ion interactions on the IR spectrum of benzenesulfonate ion. Restoration of sulfonate ion symmetry in sodium benzenesulfonate dimer, *J. Mol. Struct.*, 2016, **1123**, 360–366.

52 P. Chen, H. Zhu, T. Na, Y. Yi, J. Zhou, T. Duan and J. Lei, Functionalized collagen fiber with specific recognition sites for highly efficient iodine capture: theoretical calculations and experimental verification, *Chem. Eng. J.*, 2023, **476**, 146660.

53 Y. Xie, Q. Rong, F. Mao, S. Wang, Y. Wu, X. Liu, M. Hao, Z. Chen, H. Yang, G. I. N. Waterhouse, S. Ma and X. Wang, Engineering the pore environment of antiparallel stacked covalent organic frameworks for capture of iodine pollutants, *Nat. Commun.*, 2024, **15**, 2671.

54 Y. Sun, S. Song, D. Xiao, L. Gan and Y. Wang, Easily constructed imine-bonded COFs for iodine capture at ambient temperature, *ACS Omega*, 2020, **5**, 24262–24271.

55 Y. Chen, X. Song, A. Li, Z. Song, S. Fu, Y. Xie, B. Z. Tang and Z. Li, Solvent-responsive nonporous adaptive crystals derived from pyridinium hydrochloride and the application in iodine adsorption, *Adv. Mater.*, 2024, **36**, 2402885.

56 M. Zahid, D. Zhang, X. Xu, M. Pan, M. H. ul Haq, A. T. Reda and W. Xu, Barbituric and thiobarbituric acid-based UiO-66-NH_2 adsorbents for iodine gas capture: Characterization, efficiency and mechanisms, *J. Hazard. Mater.*, 2021, **416**, 125835.

57 Y. Li, Y. Li, Q. Zhao, L. Li, R. Chen and C. He, Cotton fiber functionalized with 2D covalent organic frameworks for iodine capture, *Cellulose*, 2019, **27**, 1517–1529.

58 B. Wu, Z.-W. Li, F. Lin, R. Tang, W. Zhang, H. Liu, G. Ouyang and Y. Tan, The paradigm for exceptional iodine capture by nonporous amorphous electron-deficient cyclophanes, *J. Hazard. Mater.*, 2024, **465**, 133449.

59 L. Zhang, J. Li, H. Zhang, Y. Liu, Y. Cui, F. Jin, K. Wang, G. Liu, Y. Zhao and Y. Zeng, High iodine uptake in two-dimensional covalent organic frameworks, *Chem. Commun.*, 2021, **57**, 5558–5561.

60 Y. Zhang, L. He, T. Pan, J. Xie, F. Wu, X. Dong, X. Wang, L. Chen, S. Gong, W. Liu, L. Kang, J. Chen, L. Chen, L. Chen, Y. Han and S. Wang, Superior iodine uptake capacity enabled by an open metal-sulfide framework composed of three types of active sites, *CCS Chem.*, 2022, **5**, 1540–1548.